nature physics

LETTERS

PUBLISHED ONLINE: 4 APRIL 2016 | DOI: 10.1038/NPHYS3712

Dirac node arcs in $PtSn_4$

Yun Wu[1,2], Lin-Lin Wang[1], Eundeok Mun[1,2†], D. D. Johnson[1,2,3], Daixiang Mou[1,2], Lunan Huang[1,2], Yongbin Lee[1], S. L. Bud'ko[1,2], P. C. Canfield[1,2*] and Adam Kaminski[1,2*]

In topological quantum materials[1–3] the conduction and valence bands are connected at points or along lines in the momentum space. A number of studies have demonstrated that several materials are indeed Dirac/Weyl semimetals[4–8]. However, there is still no experimental confirmation of materials with line nodes, in which the Dirac nodes form closed loops in the momentum space[2,3]. Here we report the discovery of a novel topological structure—Dirac node arcs—in the ultrahigh magnetoresistive material $PtSn_4$ using laser-based angle-resolved photoemission spectroscopy data and density functional theory calculations. Unlike the closed loops of line nodes, the Dirac node arc structure arises owing to the surface states and resembles the Dirac dispersion in graphene that is extended along a short line in the momentum space. We propose that this reported Dirac node arc structure is a novel topological state that provides an exciting platform for studying the exotic properties of Dirac fermions.

The discovery of nontrivial surface states in topological insulators[1] has attracted a lot of interest and initiated quests for diverse novel topological states in condensed matter. Topological nodal states with conduction and valence bands touching at points (Dirac/Weyl semimetals) or lines (line node semimetals) have been proposed to exist in multilayer heterostructures[2]. A possible extension of these states to three dimensional (3D) single crystals was proposed in β-cristobalite BiO_2(ref. 9) and A_3Bi (A = Na, K, Rb; ref. 10), which are thought to host bulk 3D Dirac points protected by crystal symmetry. Subsequently, Na_3Bi and Cd_3As_2 were experimentally demonstrated to be 3D Dirac semimetals[4,5,11,12]. Subsequently, another type of massless particle—the Weyl fermion[13]—was found in states that were predicted to exist in a family of non-centrosymmetric transition metal TaAs, TaP, NbP and NbAs (refs 14,15). These materials were confirmed as Weyl semimetals by reports of Fermi arc states connecting the Weyl points as a unique signature[6–8]. Although experimental evidence supports the existence of Dirac semimetals and Weyl semimetals, clear signatures of semimetals with line nodes are yet to be discovered. Several groups proposed that line node structures may exist in graphene networks[16], rare earth monopnictides[17], antiperovskite Cu_3PdN/Cu_3ZnN (refs 18,19), $SrIrO_3$ (ref. 20), $TlTaSe_2$ (ref. 21), Ca_3P_2 (ref. 22) and $CaAgX$(X = P, As; ref. 23), but so far no direct evidence has been reported. Several angle-resolved photoemission spectroscopy (ARPES) studies in $PbTaSe_2$ (ref. 24) and ZrSiS (ref. 25) presented some evidence of the existence of Dirac-like features and 'drumhead' surface states, but further research is still needed to understand fully their significance and relation to Dirac line nodes.

Many topological nodal semimetals, such as Cd_3As_2 (ref. 26), NbP (ref. 27) and WTe_2 (ref. 28), exhibit extremely large magnetoresistance. Before these discoveries, a similar effect was observed in $PtSn_4$, with a magnetoresistance of $\simeq 5 \times 10^5$% and no obvious saturation at 1.8 K and 140 kOe (ref. 29). However, the band structure of this material has not been studied experimentally in detail owing to the very complex Fermi surface (FS) revealed by calculations[29]. Here we demonstrate that, despite its complex FS in the centre region of the Brillouin zone, there are also very interesting features close to the boundary of the zone, that is, the Z and X points, which are the signatures of a topological quantum material. Whereas most of the topological quantum materials were predicted by theory first and verified by experiment later, we present an opposite approach: we focused on ultrahigh non-saturating magnetoresistance, and on this basis we searched for topological states in $PtSn_4$ by means of ultrahigh resolution ARPES, followed with band structure calculations.

The crystal structure, Fermi surface and band dispersion along key directions in the Brillouin zone (BZ) for $PtSn_4$ are shown in Fig. 1. Figure 1b shows the ARPES intensity integrated within 10 meV of the chemical potential. High-intensity areas mark the contours of the FS sheets. The FS consists of at least one large electron pocket at the centre of BZ, surrounded by several other electron and hole FS sheets, consistent with the quantum oscillation result[29]. Figure 1c shows the calculated bulk FS, which matches the data well close to the centre of the zone and Z point in Fig. 1b, and is also consistent with the calculated FS using the full potential linearized augmented plane wave (FLAPW) method within the local density approximation (LDA; ref. 29). However, it does not predict the FS crossings close to the X point, missing a set of nearly parallel FS sheets that are present in Fig. 1b. On the other hand, these experimental features are reproduced well by a calculation of the surface states using the slab method; results of which are shown in Fig. 1d. Band dispersions along several cuts in proximity to the Z and X points are shown in Fig. 1e–l. Close to the Z point (Fig. 1e,g), the dispersion resembles a Dirac-like feature, but the intensity within the band contour indicates a bulk origin and is consistent with corresponding band calculations shown in Fig. 1f,h. Close to the X point (Fig. 1i,k), the band dispersion is also Dirac-like, but very sharp, and thus more likely to be due to surface states; moreover, it is consistent with the slab calculation shown in Fig. 1j,l. The data in Fig. 1 demonstrate that the experimentally observed band structure has both bulk and surface components. The former dominate the Fermi surface close to the Z point, and the latter is prominent close to the X point. The linear dispersion and gapless band crossings strongly suggest that both bulk and surface features at the edge of the Brillouin zone may have topological character, possibly linked to the ultrahigh magnetoresistance, similar to Cd_3As_2 (ref. 5), NbP (ref. 8) and WTe_2 (ref. 30).

[1]Division of Materials Science and Engineering, Ames Laboratory, Ames, Iowa 50011, USA. [2]Department of Physics and Astronomy, Iowa State University, Ames, Iowa 50011, USA. [3]Department of Materials Science and Engineering, Iowa State University, Ames, Iowa 50011, USA. †Present address: Department of Physics, Simon Fraser University, Burnaby, British Columbia V5A 1S6, Canada. *e-mail: canfield@ameslab.gov; kaminski@ameslab.gov

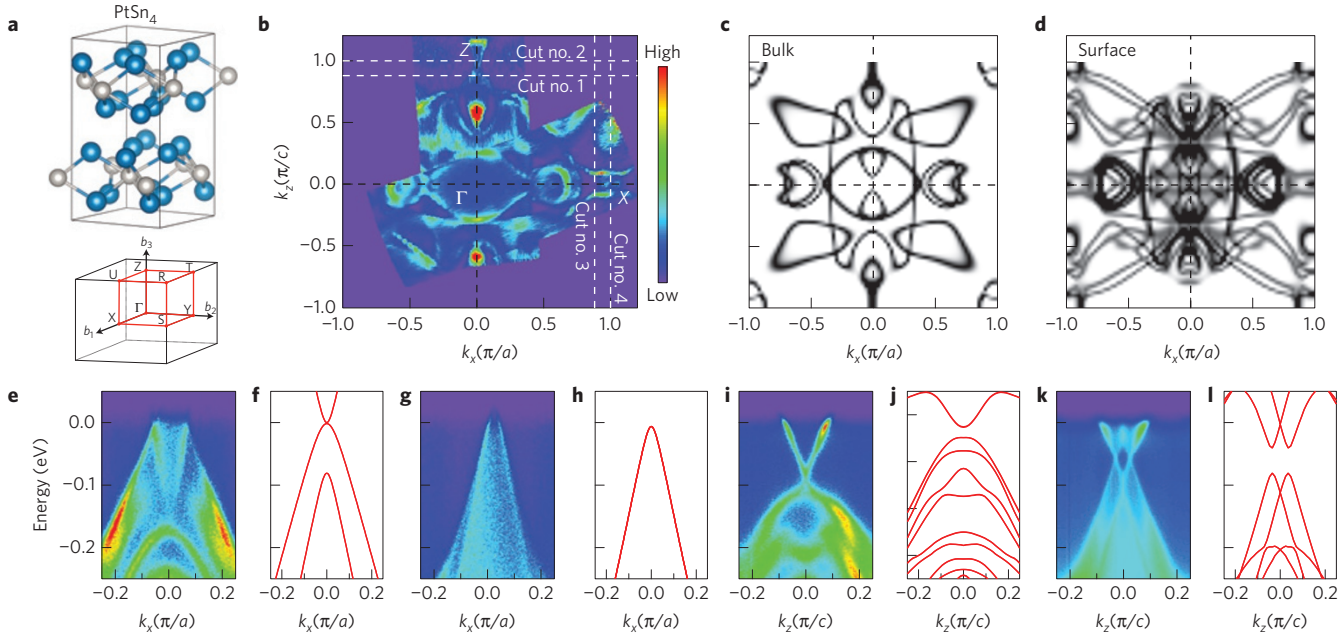

Figure 1 | Experimental and calculated structure of the Fermi surface and band dispersion of $PtSn_4$. **a**, Crystal structure (Pt, white spheres; Sn, blue spheres) and Brillouin zone of $PtSn_4$. **b**, Fermi-surface plot of the ARPES intensity integrated within 10 meV of the chemical potential along $\Gamma-Z$ and $\Gamma-X$. **c**, Bulk FS slice calculated by density functional theory (DFT) at $k_y = 0.284\pi/b$. **d**, Calculated surface FS with a 24-layer slab. **e**, Band dispersion at $k_z = 0.88\pi/c$ along cut no. 1 in **b**. **f**, Calculated bulk-band dispersion at $k_z = 0.88\pi/c$ and $k_y = 0.284\pi/b$. **g**, Band dispersion at $k_z = \pi/c$ along cut no. 2 in **b**. **h**, Calculated bulk-band dispersion at $k_z = \pi/c$ and $k_y = 0.284\pi/b$. **i**, Band dispersion at $k_x = 0.88\pi/a$ along cut no. 3 in **b**. **j**, Calculated surface-band dispersion at $k_x = 0.88\pi/a$ with a 42-layer slab. **k**, Band dispersion at $k_x = \pi/a$ along cut no. 4 in **b**. **l**, Calculated surface-band dispersion at $k_x = \pi/a$ with a 42-layer slab.

In Fig. 2 we focus on the interesting features near the Z point in more detail. An enlarged image from the red box in Fig. 2a is shown in panel b, where two triangular-shaped FS sheets are observed. The detailed evolution of band dispersions along cuts no. 1 to no. 8 is shown in Fig. 2c. A sharp linear dispersion starts to cross at a binding energy of ∼200 meV in cut no. 1, and the Dirac point moves up in energy in cuts no. 2–no. 5, finally reaching the Fermi level in cut no. 6, as indicated by red arrows. Then, the Dirac point moves up above the Fermi level and becomes a sharp, shallow hole pocket in cuts no. 7 and no. 8. This movement of the Dirac nodes forms a line in the energy–momentum space in the proximity of Z.

Whereas the behaviour described above has previously been predicted by theory, the structure in the proximity of the X point is far more interesting. We now examine the Fermi surface and band dispersion in a small area in the part of the Brillouin zone that is marked by the red box in Fig. 3a. The Fermi surface in this region consists of a short arc along the symmetry line and two longer, nearly parallel segments on either side of this arc. Detailed band dispersion along cuts no. 1 to no. 12 are shown in Fig. 3c. The data along cut no. 1 show Dirac-like dispersion, with the top and bottom bands merging at a single gapless point. The band is very sharp, consistent with its surface origin. As we move closer to the X point, two things happen: a gap develops between top and bottom bands and both top and bottom bands split into two parts symmetric about the $k_z = 0$ line (cuts no. 2–no. 4). Before reaching the X point, the gap vanishes and there are two gapless Dirac-like features in close proximity to the X point. The inner bands of the two Dirac features merge along the symmetry line and form an arc at the chemical potential visible in Fig. 3b. The two gapless, Dirac-like features extend along one direction in the proximity of the X point between $k_x \approx 0.95\pi/a$ and $1.05\pi/a$ (cuts no. 5 and no. 10 marked by the red frame in Fig. 3c). Outside this momentum range a gap develops, separating the upper and lower portion of the band that is, cuts no. 4.5 and no. 10.5 are already gapped. This gives rise to two arcs of Dirac nodes located at a binding energy of ∼60 meV, one on each side of the Γ–X symmetry line, which we named Dirac node arcs.

We now proceed to demonstrate that the Dirac-like dispersion shown in Fig. 3 is gapless by plotting the momentum dispersion curves (MDCs) and energy dispersion curves (EDCs). Figure 4c shows the EDC extracted along the red dashed line in 4b. The red arrow marks the peak located at roughly 90 meV below the Fermi level (Fig. 4a), and demonstrates the absence of an energy gap in this single Dirac-like feature. In Fig. 4d, we show the double Dirac-like features along cut no. 8 (Fig. 3c). The EDCs shown in 4f are extracted along the red dashed lines marked as 1, 2, 3 in Fig. 4e. The red arrows in Fig. 4e,f mark the locations of the peaks at a binding energy of ∼60 meV, and show the gapless nature of these dispersions. The same cut measured at two other photon energies (6.36 eV and 6.05 eV) is shown in Fig. 4g and h, respectively. It is clear that the band dispersion does not vary with the incident photon energy (within 16% of the Brillouin zone), demonstrating its surface origin. As such, those states do not have dispersion along a direction perpendicular to the sample surface (that is, k_y). The surface-state calculation using a 42-layer slab shows that the conduction and valence bands are separated by roughly 23 meV in the single Dirac feature. However, a further increase in the layer number reduces the gap size significantly, as shown in Fig. 4j. To better illustrate the Dirac node arc structure, we plot the location of the Dirac nodes in momentum space in Fig. 4k by extracting the peak positions of the MDCs at each node (that is, at a binding energy of 90 meV in the single Dirac dispersion and 60 meV at the proximity of the X point in the double Dirac dispersion, as marked by the red dashed lines in Fig. 4a,d). In Fig. 4l, the schematic of the double Dirac node arc structure is shown, with two Dirac dispersions extending along one dimension in momentum space.

Our results show that, near the X point, the single Dirac dispersion evolves into two gapped dispersions and, before reaching

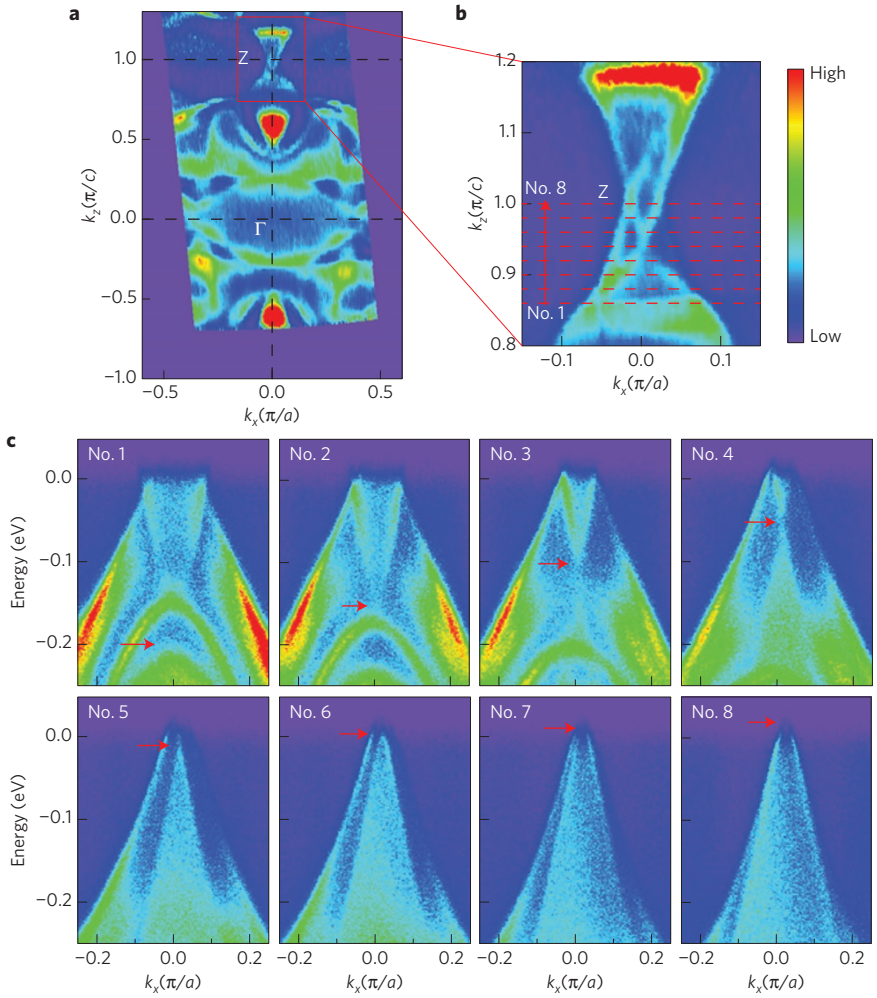

Figure 2 | Fermi surface and band dispersion in the proximity of the Z point. a, Fermi surface plot of the ARPES intensity integrated within 10 meV of the chemical potential along Γ − Z. **b**, Zoomed image of the red box in **a**, red dashed lines mark cuts no. 1–no. 8. **c**, Band dispersion along cuts no. 1–no. 8. Cut no. 8 passes through the Z point. The red arrows mark the Dirac nodes.

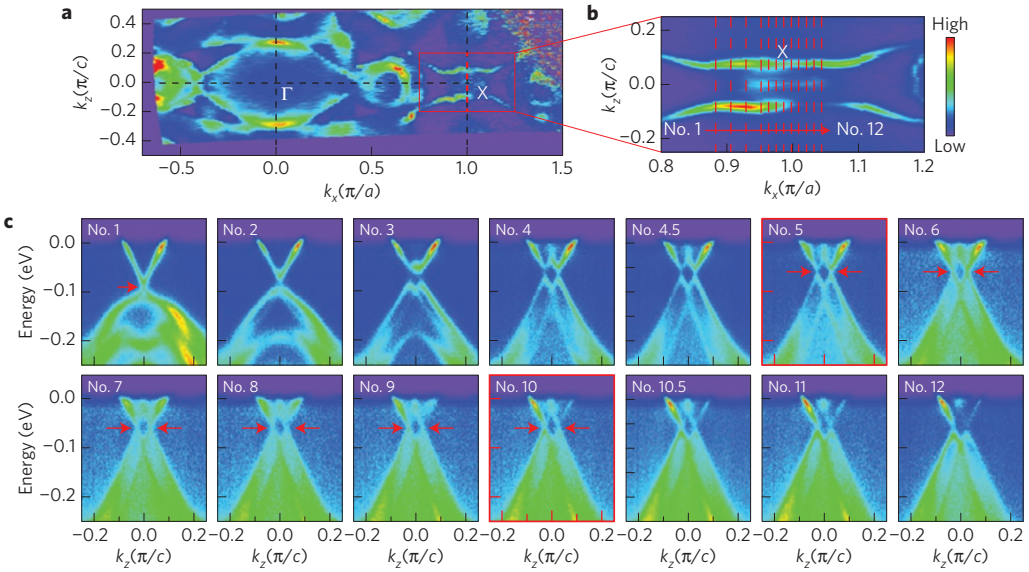

Figure 3 | Fermi surface plot and band dispersion close to the X point. a, Fermi surface plot of the ARPES intensity integrated within 10 meV of the chemical potential along Γ − X. **b**, Zoomed image of the red box in **a**, red dashed lines mark cuts no. 1–no. 12. **c**, Band dispersion along cuts no. 1–no. 12. Cut no. 8 passes through the X point. The red arrows mark the Dirac nodes. Cuts no. 5 and no. 10 (boxes edged in red) are the dispersions at the end points of the Dirac node arcs.

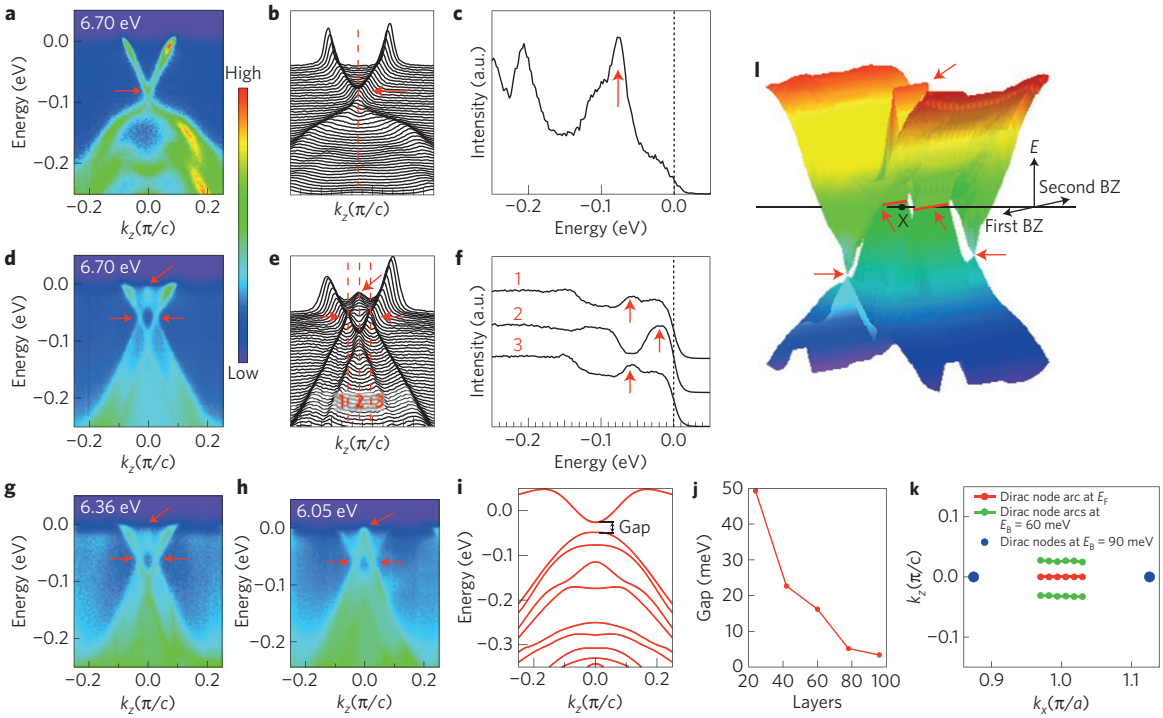

Figure 4 | Two types of gapless Dirac-like dispersion close to the X point. a, Band dispersion along cut no. 1 in Fig. 3b measured at a photon energy of 6.70 eV. **b**, Momentum dispersion curves (MDC) of **a**. **c**, Energy dispersion curve (EDC) along the red dashed line in **b**. **d**, Band dispersion along cut no. 8 in Fig. 3b measured at a photon energy of 6.70 eV. **e**, Momentum dispersion curves (MDC) of **d**. **f**, Energy dispersion curves (EDC) along the red dashed lines in **e**. **g**, Band dispersion along cut no. 8 in Fig. 3b measured at a photon energy of 6.36 eV. **h**, Band dispersion along cut no. 8 in Fig. 3b measured at a photon energy of 6.05 eV. **i**, Calculated surface band along a cut at $k_x = 0.88\pi/a$, similar to cut no. 3 in **b**, with a 42-layer slab. **j**, Evolution of the energy gap with an increasing number of layers in the slab. **k**, Locations of the Dirac nodes extracted from the peak positions of the MDCs as marked by the horizontal red arrows in **a** and **d**. The blue dots denote the two single Dirac nodes at $E_B \sim 90$ meV. The green dots denote the two Dirac node arcs at $E_B \sim 60$ meV. The red dots denote the Dirac node arc at E_F. **l**, Schematic of the double Dirac node arc structure. Red arrows mark the double single nodes and double node arcs.

the X point, the gaps close and two gapless Dirac-like feature emerge extending along one dimension in momentum space, forming a Dirac node arc. These novel features differ from previously predicted Dirac line nodes that form closed loops in momentum space. We proposed that this novel topological nodal structure could be an ideal platform for studying the exotic properties of Dirac fermions. Finally, we note that most of the recently discovered ultrahigh magnetoresistive materials[26–28] seem to also possess Dirac or Weyl features in the band dispersions[5,8,30]. As we have demonstrated, this opens an avenue for discovering and identifying novel topological states and relativistic behaviour based on rudimentary transport measurements.

Methods

Methods, including statements of data availability and any associated accession codes and references, are available in the online version of this paper.

Received 14 December 2015; accepted 1 March 2016; published online 4 April 2016; corrected online 7 April 2016

References

1. Hasan, M. Z. & Kane, C. L. Colloquium: topological insulators. *Rev. Mod. Phys.* **82,** 3045–3067 (2010).
2. Burkov, A. A., Hook, M. D. & Balents, L. Topological nodal semimetals. *Phys. Rev. B* **84,** 235126 (2011).
3. Heikkil, T. & Volovik, G. Dimensional crossover in topological matter: evolution of the multiple dirac point in the layered system to the flat band on the surface. *JETP Lett.* **93,** 59–65 (2011).
4. Liu, Z. K. *et al*. Discovery of a three-dimensional topological Dirac semimetal, Na_3Bi. *Science* **343,** 864–867 (2014).
5. Neupane, M. *et al*. Observation of a three-dimensional topological Dirac semimetal phase in high-mobility Cd_3As_2. *Nature Commun.* **5,** 3786 (2014).
6. Xu, S.-Y. *et al*. Discovery of a Weyl fermion semimetal and topological Fermi arcs. *Science* **349,** 613–617 (2015).
7. Xu, S. *et al*. Discovery of a Weyl fermion state with Fermi arcs in niobium arsenide. *Nature Phys.* **11,** 748–754 (2015).
8. Xu, S.-Y. *et al*. Experimental discovery of a topological Weyl semimetal state in TaP. *Sci. Adv.* **1,** e1501092 (2015).
9. Young, S. M. *et al*. Dirac semimetal in three dimensions. *Phys. Rev. Lett.* **108,** 140405 (2012).
10. Wang, Z. *et al*. Dirac semimetal and topological phase transitions in A_3Bi (A = Na, K, Rb). *Phys. Rev. B* **85,** 195320 (2012).
11. Wang, Z., Weng, H., Wu, Q., Dai, X. & Fang, Z. Three-dimensional Dirac semimetal and quantum transport in Cd_3As_2. *Phys. Rev. B* **88,** 125427 (2013).
12. Liu, Z. K. *et al*. A stable three-dimensional topological Dirac semimetal Cd_33As_2. *Nature Mater.* **13,** 677–681 (2014).
13. Weyl, H. Elektron und gravitation. i. *Z. Phys.* **56,** 330–352 (1929).
14. Huang, S. *et al*. A Weyl fermion semimetal with surface Fermi arcs in the transition metal monopnictide TaAs class. *Nature Commun.* **6,** 7373 (2015).
15. Weng, H., Fang, C., Fang, Z., Bernevig, B. A. & Dai, X. Weyl semimetal phase in noncentrosymmetric transition-metal monophosphides. *Phys. Rev. X* **5,** 011029 (2015).
16. Weng, H. *et al*. Topological node-line semimetal in three-dimensional graphene networks. *Phys. Rev. B* **92,** 045108 (2015).
17. Zeng, M. *et al*. Topological semimetals and topological insulators in rare earth monopnictides. Preprint at http://arxiv.org/abs/1504.03492 (2015).
18. Yu, R., Weng, H., Fang, Z., Dai, X. & Hu, X. Topological node-line semimetal and Dirac semimetal state in antiperovskite Cu_3PdN. *Phys. Rev. Lett.* **115,** 036807 (2015).
19. Kim, Y., Wieder, B. J., Kane, C. L. & Rappe, A. M. Dirac line nodes in inversion-symmetric crystals. *Phys. Rev. Lett.* **115,** 036806 (2015).
20. Fang, C., Chen, Y., Kee, H-Y. & Fu, L. Topological nodal line semimetals with and without spin-orbital coupling. *Phys. Rev. B* **92,** 081201 (2015).
21. Bian, G. *et al*. Drumhead surface states and topological nodal-line fermions in $TlTaSe_2$. Preprint at http://arxiv.org/abs/1508.07521 (2015).

22. Xie, L. S. *et al*. A new form of Ca_3P_2 with a ring of Dirac nodes. *APL Mater.* **3,** 083602 (2015).
23. Yamakage, A., Yamakawa, Y., Tanaka, Y. & Okamoto, Y. Line-node Dirac semimetal and topological insulating phase in noncentrosymmetric pnictides CaAgX (X = P, As). *J. Phys. Soc. Jpn* **85,** 013708 (2016).
24. Bian, G. *et al*. Topological nodal-line fermions in spin-orbit metal $PbTaSe_2$. *Nature Commun.* **7,** 10556 (2016).
25. Schoop, L. M. *et al*. Dirac cone protected by non-symmorphic symmetry and 3D Dirac line node in ZrSiS. Preprint at http://arxiv.org/abs/1509.00861 (2015).
26. Liang, T. *et al*. Ultrahigh mobility and giant magnetoresistance in the Dirac semimetal Cd_3As_2. *Nature Mater.* **14,** 280–284 (2015).
27. Shekhar, C. *et al*. Extremely large magnetoresistance and ultrahigh mobility in the topological Weyl semimetal candidate NbP. *Nature Phys.* **11,** 645–649 (2015).
28. Ali, M. N. *et al*. Large, non-saturating magnetoresistance in WTe_2. *Nature* **514,** 205–208 (2014).
29. Mun, E. *et al*. Magnetic field effects on transport properties of $PtSn_4$. *Phys. Rev. B* **85,** 035135 (2012).
30. Wu, Y. *et al*. Temperature-induced Lifshitz transition in WTe_2. *Phys. Rev. Lett.* **115,** 166602 (2015).

Acknowledgements

This work was supported by the US Department of Energy, Office of Science, Basic Energy Sciences, Materials Science and Engineering Division. Ames Laboratory is operated for the US Department of Energy by Iowa State University under contract No. DE-AC02-07CH11358.

Author contributions

P.C.C. initiated the work by insisting that Y.W. and A.K. design and carry out the experiment. Y.W., D.M. and L.H. acquired and analysed ARPES data. L.-L.W., D.D.J. and Y.L. carried out the DFT calculations. E.M. grew the samples under the supervision of S.L.B. and P.C.C. The manuscript was drafted by Y.W. and A.K. All authors discussed and commented on the manuscript.

Additional information

Reprints and permissions information is available online at www.nature.com/reprints. Correspondence and requests for materials should be addressed to P.C.C. or A.K.

Competing financial interests

The authors declare no competing financial interests.

Methods

Sample growth. Single crystals of $PtSn_4$ were grown out of a Sn-rich binary melt[31]. The constituent elements, with an initial stoichiometry of $Pt_{0.04}Sn_{0.96}$, were placed in an alumina crucible and sealed in a quartz tube under a partial Ar pressure. After the quartz ampoule was heated up to 600 °C, the ampoule was cooled down to 350 °C over 60 h (ref. 29). To decant the Sn readily at this temperature, a frit-disc crucible was used[32].

Sample preparation and measurements. ARPES measurements were carried out using a laboratory-based system consisting of a Scienta R8000 electron analyser and a tunable vacuum ultraviolet laser light source[33]. The data were acquired using a tunable vacuum ultraviolet laser ARPES system, consisting of a Scienta R8000 electron analyser, picosecond Ti:sapphire oscillator and fourth harmonic generator. All data were collected with a constant photon energy of 6.7 eV, except for Fig. 4g (6.36 eV) and 4h (6.05 eV). The angular resolution was set at ∼0.05° and 0.5° (0.005 $Å^{-1}$ and 0.05 $Å^{-1}$) along and perpendicular to the direction of the analyser slit (and thus the cut in the momentum space), respectively; energy resolution was set at 1 meV. The size of the photon beam on the sample was ∼30 µm. Samples were cleaved *in situ* at a base pressure lower than 1×10^{-10} torr. Samples were cooled using a closed-cycle He refrigerator and the sample temperature was measured using a silicon-diode sensor mounted on the sample holder. The energy corresponding to the chemical potential was determined from the Fermi edge of a polycrystalline Au reference in electrical contact with the sample. Samples were cleaved at 40 K and were kept at the cleaving temperature throughout the measurement.

Calculation method. Density functional theory[34,35] (DFT) calculations were done in the Vienna *Ab initio* Simulation Package (VASP; refs 36,37) using the Perdew–Burke–Ernzerhof (PBE; ref. 38) exchange–correlation functional, a plane-wave basis set with projected augmented waves[39] and the spin–orbital coupling (SOC) effect included. For the bulk-band structure of $PtSn_4$, we use the conventional orthorhombic cell of 20 atoms with a Monkhorst–Pack[40] $(8 \times 6 \times 8)$ *k*-point mesh. For surface-band structure, we use slabs up to 96 atomic layers or 320 atoms with a $(8 \times 1 \times 8)$ k-point mesh and at least a 12 Å vacuum. The kinetic energy cutoff is 230 eV. The convergence with respect to the k-point mesh was carefully checked, with total energy converged, for example, well below 1 meV/atom. We use experimental lattice parameters[41] of $a = 6.418$ Å, $b = 11.366$ Å and $c = 6.384$ Å with atoms fixed in their bulk positions.

Data availability. Raw data for this manuscript is available at http://lib.dr.iastate.edu/ameslab_datasets/2.

References

31. Canfield, P. C. & Fisk, Z. Growth of single crystals from metallic fluxes. *Philos. Mag.* **65,** 1117–1123 (1992).
32. Canfield, P. C., Kong, T., Kaluarachchi, U. S. & Jo, N. H. Use of frit-disc crucibles for routine and exploratory solution growth of single crystalline samples. *Philos. Mag.* **96,** 84–92 (2016).
33. Jiang, R. *et al*. Tunable vacuum ultraviolet laser based spectrometer for angle resolved photoemission spectroscopy. *Rev. Sci. Instrum.* **85,** 033902 (2014).
34. Hohenberg, P. & Kohn, W. Inhomogeneous electron gas. *Phys. Rev.* **136,** B864–B871 (1964).
35. Kohn, W. & Sham, L. J. Self-consistent equations including exchange and correlation effects. *Phys. Rev.* **140,** A1133–A1138 (1965).
36. Kresse, G. & Furthmüller, J. Efficient iterative schemes for *ab initio* total-energy calculations using a plane-wave basis set. *Phys. Rev. B* **54,** 11169–11186 (1996).
37. Kresse, G. & Furthmller, J. Efficiency of *ab-initio* total energy calculations for metals and semiconductors using a plane-wave basis set. *Comput. Mater. Sci.* **6,** 15–50 (1996).
38. Perdew, J. P., Burke, K. & Ernzerhof, M. Generalized gradient approximation made simple. *Phys. Rev. Lett.* **77,** 3865–3868 (1996).
39. Blöchl, P. E. Projector augmented-wave method. *Phys. Rev. B* **50,** 17953–17979 (1994).
40. Monkhorst, H. J. & Pack, J. D. Special points for Brillouin-zone integrations. *Phys. Rev. B* **13,** 5188–5192 (1976).
41. Knnen, B., Niepmann, D. & Jeitschko, W. Structure refinements and some properties of the transition metal stannides Os_3Sn_7, Ir_5Sn_7, $Ni_{0.402(4)}Pd_{0.598}Sn_4$, α-$PdSn_2$ and $PtSn_4$. *J. Alloys Compd.* **309,** 1–9 (2000).